CrossMark

Structural, Optical, Thermal and Photocatalytic Dye Degradation Properties of BiFeO$_3$–WO$_3$ Nanocomposites

YATHAVAN SUBRAMANIAN,[1] VENKATAPATHY RAMASAMY,[1]
RAMESH KUMAR GUBENDIRAN,[1,4] GOKUL RAJ SRINIVASAN,[2]
and DURAIRAJAN ARULMOZHI[3]

1.—Department of Physics, University College of Engineering Arni, Anna University, Arni, India.
2.—Department of Physics, C. Kandaswami Naidu College for Men, Chennai, India. 3.—I3N-Aveiro, Department of Physics, University of Aveiro, Aveiro, Portugal. 4.—e-mail: rameshvandhai@gmail.com

In the present work, nanocomposites of BiFeO$_3$–WO$_3$ (BFO–WO$_3$) have been successfully synthesized for the first time by a single step sol–gel method. The main objective lies in enhancing the photocatalytic activity of BiFeO$_3$ by modifying it with a WO$_3$ matrix. Powder x-ray diffraction studies on BFO–WO$_3$ confirm the presence of the monoclinic character of WO$_3$ along with rhombohedral BFO. In addition, elemental mapping using energy dispersive x-ray analysis ascertains the existence of tungsten ions in the BFO matrix. Field emission scanning electron microscopy analysis on pure and nanocomposites depicts the distinct morphologies of the nanoparticles upon modification of BFO with WO$_3$. From the UV–Vis–NIR spectrum, it has been noticed that there is a reduction in the band gap energy from 1.8 eV (BFO) to 1.5 eV (BFO–WO$_3$) suggesting the increase in the absorption of a visible portion of light upon loading of WO$_3$ in BFO. Thermogravimetric analysis/differential thermal analysis trace of BFO–WO$_3$ nanocomposites shows that there is a suppression of the multiferroic character of BiFeO$_3$, when it is modified with WO$_3$. However, the photodegradation of methylene blue using BFO–WO$_3$ nanoparticles found to have been enhanced to 91%. The increase in dye removal property may be due to the fact that the higher surface area of nanocomposites due to the incorporation of WO$_3$ particles. The other significant results have been discussed in detail.

Key words: Methylene blue, dye degradation, nanocomposites

INTRODUCTION

Recently, semiconductor photocatalysts have been given considerable attention among the scientific community due to their property of complete decomposition of the harmful pollutants from usable water resources and solar energy.[1] As solar light can be a potential energy source for photocatalytic degradation, initial researches on the semiconductor based photocatalysis were focused mainly on wide band gap semiconductors like TiO$_2$, titanates,

etc., using UV light, and it was observed by Fuishima and Honda[2] owing to their high stability, low cost, and nontoxicity. However, their application in photocatalysis under visible light is limited, consequent to their large band gap energy of 3.0–3.4 eV, which could activate only the UV portion of light.[3–6] Many attempts, including doping with metals and/or nonmetals, attaching dye molecules as the photosensitizers, were found to have been carried out to make them visible light active.[7] But, it has ended up with limited success. In case of doping with metals and/or nonmetals, extending the light absorption towards the visible region was too little and interband doping states act as the source of recombination centers for the photogenerated

electrons and holes limiting the objective of doping.[8] Therefore, focus has now been shifted towards the semiconductors (e.g., CdS, Cu$_2$O etc.) with narrow band gap energy, which is quite active in the visible light region. CdS was the most popular among them due to its appropriate band gap of 2.4 eV for the visible light harvesting and also for more negative conduction band edge position as compared to the H$^+$/H$_2$ redox potential.[9,10] However, the major drawback for CdS is that it is very susceptible to photocorrosion.[11] Hence, there is a need to design a visible light active photocatalyst with greater stability and to act as a viable alternative to the TiO$_2$ and CdS based materials. It is widely accepted that BiFeO$_3$[12,13] is a promising material with potential applications in many advanced fields including piezoelectric devices, photovoltaics and photocatalysis. It has a narrow band gap (2.1–2.7 eV),[14] and it is found to be lower than the other Bi based photocatalytic systems such as Bi$_2$WO$_6$ and Bi$_2$W$_2$O$_9$, BiVO$_4$.[15–20] Indeed, BiFeO$_3$ based materials have become the choice as photocatalyst for the degradation of organic pollutants from aqueous media as well as for water splitting reactions under visible light irradiations. In fact, BiFeO$_3$ has been modified by doping with metals, loading with a co-catalyst and by heterojunction formation to improve its surface area, light absorptivity and charge carrier separation properties.[21–24] For example, La^{3+} and Se^{4+} co-doped bismuth ferrite nanostructures exhibit excellent photocatalytic activity for the degradation of congo red dye and acetophenone which has been ascribed to the improved optical absorption, charge carrier separation and migration.[25] Further, heterogenous photocatalyts are found to be displaying higher photo induced charge separation and greater photocatalytic efficiency.[26,27] BiFeO$_3$ based type heterogeneous photocatalyts including BiFeO$_3$/g-C$_3$N$_4$, BiFeO$_3$/CuWO$_4$ and BiFeO$_3$/ZnFe$_2$O$_4$[28–34] substantiates the significance of photocatalytic activity of BFO based compounds. These heterojunction systems could show better photocatalytic activity for the degradation of organic dye in aqueous medium, but their ability is limited due to the quick charge recombination. On the other hand, WO$_3$ is a narrow band gap semiconducting material (2.4–2.9 eV) with potential visible light absorption properties and photocatalytic activity.[35–39] WO$_3$/TiO$_2$ and g-C$_3$N$_4$/WO$_3$ are some of the recently studied heterojunction materials which have shown improved catalytic performance for hydrogen production and organic dye removal.[40–42] WO$_3$ happens to be a natural choice to form a heterojunction with Bi based semiconducting materials due to its higher positive conduction band and valence band potentials. Bi based semiconducting compounds such as BiFeO$_3$, exhibit low positive conduction band potential. Hence, the combination of two visible light active materials can be an efficient heterogeneous type system with improved photon harvesting property and higher photocatalytic activity with greater stability. With an intention to develop novel and sustainable visible light induced photocatalysts, we have made an attempt to synthesize BiFeO$_3$/WO$_3$ heterojunction nanomaterials and have studied their improved photocatalytic activity for the degradation of methylene blue from aqueous solution using natural sunlight. To the best of our knowledge, there is no report on photocatalytic degradation of methylene blue using BiFeO$_3$/WO$_3$ heterojunction photocatalyst.

EXPERIMENTAL PROCEDURE

All the purchased chemicals were of analytical grade (AR) and used as received without further purification. The precursors used were bismuth nitrate pentahydrate (Merck—99% purity), iron nitrate nano hydrate (Merck—98% purity), Conc. HNO$_3$ (Merck—69%), tartaric acid (Merck—99%), and tungsten (VI) oxide (Merck—99%).

Synthesis of BiFeO$_3$–WO$_3$ Nanocomposites

Synthesis of BFO nanoparticles was made as per the procedure mentioned elsewhere.[43] BiFeO$_3$–WO$_3$ nanocomposite particles have been prepared from sol–gel synthesis in accordance with the procedure outlined earlier.[44,45] In a typical synthesis process as indicated in Fig. 1, 3 mmol of Bi(NO$_3$)$_3$·5H$_2$O and 3 mmol of Fe(NO$_3$)$_3$·9H$_2$O and 1 mmol of WO$_3$ were dissolved in 50 mL of distilled water. Approximately 3 mL of Conc. HNO$_3$ and 3 mmol of tartaric acid were then added to the above solution. The mixture was continuously stirred at 115°C, till it turns into a brownish solid solution. The obtained solid solution was allowed to dry at 150°C to get dry powders. Upon drying, the brown powders were calcined in a furnace at 500°C for 2 h to get BiFeO$_3$–WO$_3$ nanopowders.

Characterization Techniques Used

The structural characterization (both crystalline phase and morphology) of the synthesized photocatalysts was undertaken using a 'X'PERT PANalytical' make powder x-ray diffractometer (PXRD) in the 2θ range 10°–60° with a scan rate of 2°/min. The morphology of nanopowders has been observed through Field emission scanning electron microscope (FESEM) analysis using a S-3400N Hitachi microscope and the elemental compositions of the individual constituents Bi, W, Fe etc., have been ascertained from an energy dispersive x-ray analysis (EDX) analyser. Optical absorption spectra has been recorded with the aid of a JASCO V-670 spectrophotometer in the wavelength range of 200–800 nm. Fourier transform infrared spectroscopy (FTIR) spectra was also carried out by the KBr pellet method using a Shimadzu IR Affinity-1 spectrophotometer in the frequency range of 400–4000 cm^{-1}. Thermal measurement was recorded for BFO/WO$_3$ nanocomposite powder using a SDT Q600 V20.9 Build 20 model thermal analyser. Dye degradation properties of the chosen photocatalyst at
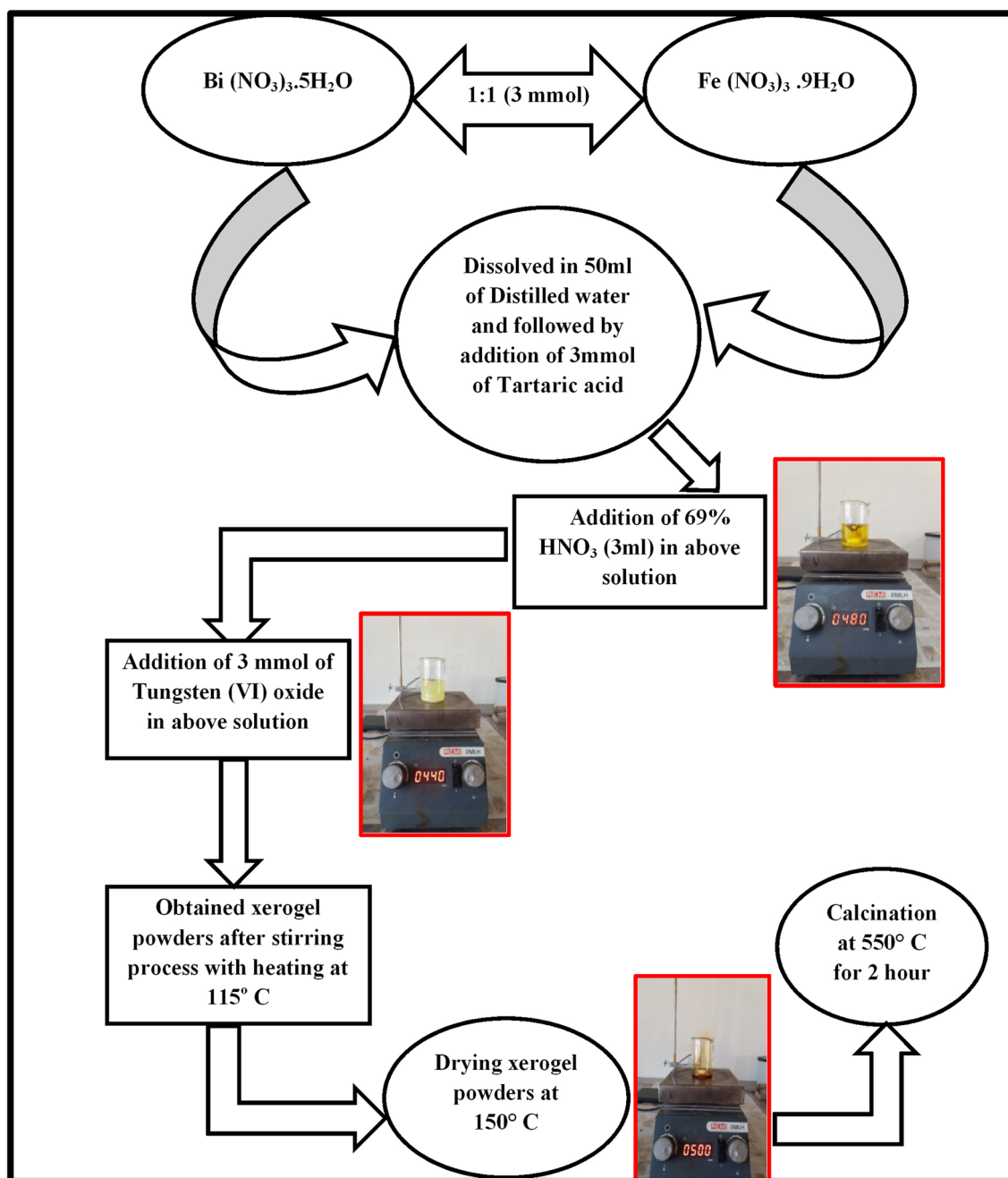
Fig. 1. Flowchart showing the steps for synthesising BFO–WO$_3$ nanocomposites from the sol–gel process.

different time intervals of study were made using a LAB INDIA double beam UV–Vis spectrophotometer (Mode no: U2900) in the wavelength range 200–800 nm. The path length was fixed as 10 mm for all trials of the experiments.

RESULTS AND DISCUSSION

Powder X-ray Diffraction (PXRD) Studies on BFO–WO$_3$ Nanocomposites

Powder XRD patterns of BFO, WO$_3$ and BiFeO$_3$–WO$_3$ photocatalysts are shown in Fig. 2. The diffraction pattern of virgin BFO indicating characteristic doublet peaks at 31.9° and 32.2° are quite consistent with the report of standard JCPDS card no. 72-2112. It corresponds to the rhombohedral phase of BFO. (hkl) planes (100) (110) (200) (210) and (2-11) indexed for BFO diffraction pattern confirm the persistence of ABO$_3$ structure. Similarly, in the case of virgin WO$_3$, low intensities peaks at 23.1°, 23.6° and 24.4° are observed, and it matches with a standard report of JCPDS card no. 84-0279. It further shows the monoclinic phase of WO$_3$, as given by Zuev et al.[46] for WO$_3$ thin films.

However, the orthorhombic character of WO$_3$ could not seen in the virgin structure, and the entire peaks of WO$_3$ reflected only the monoclinic signals.

Further, in BFO–WO$_3$ hetero-junction material, the BFO diffraction pattern present in broadened mode with low intensities was due to the possible incorporation of monoclinic WO$_3$ crystallites in addition to the increase in sizes of the particles as indexed for the well-defined peaks of BFO. A similar kind of observation was made by Bhoi et al.[47] for type-II CuS/BiFeO$_3$ heterojunctions. New peaks at 2θ values 23.1°, 23.6° and 24.4° have also been noticed due to the loading of the WO$_3$ matrix. Moderate intensities and sharp peaks indexed both for BFO and WO$_3$ suggests that nanocomposites of BFO–WO$_3$ has been well crystallised in nature. The average particle size of virgin BFO and WO$_3$ calculated from the Debye-Scherer formula was found to be $\approx$ 24 nm and 12 nm, respectively, in an isolated phase, whereas in composite phase, it has shrinked to the average size of $\approx$ 18 nm.

On perusal of the magnified view of the XRD patterns of BFO–WO$_3$ nanocomposites especially in the vicinity of 2θ around 32°, it can be seen that doublet peaks have an obvious tendency to shift towards higher 2θ values compared to BFO. This has also been invariably reflected for the rest of the peak positions. This result suggests that rhombohedral structure of the unit cell of BFO was found to have been distorted partially by WO$_3$ photocatalysts. Loading of a WO$_3$ catalyst has considerably influenced the BFO crystal structure. No impurities peaks are found in the BiFeO$_3$/WO$_3$ composites. The overall observation reveals that the photocatalyst could only be composed of the rhombohedral phase of BFO and the monoclinic moiety of WO$_3$.

In order to study crystalline strain upon loading WO$_3$ photocatalyst, Williamson–Hall (W–H)

analysis[48] was carried out for pure BFO, WO$_3$ and nanocomposite samples. The induced strain and observed changes in crystalline size have been computed using the following formalism.

$$\beta_{hkl} = \left[(\beta_{hkl})^2_{measured} - (\beta_{hkl})^2_{instrumental} \right]^{\frac{1}{2}}, \quad (1)$$

$$D = \frac{K\lambda}{\beta_{hkl} \cos \theta}, \quad (2)$$

$$\varepsilon = \frac{\beta_{hkl}}{4 \tan \theta}, \quad (3)$$

$$\beta_{hkl} = \frac{K\lambda}{D \cos \theta} + 4\varepsilon \tan \theta, \quad (4)$$

$$\beta_{hkl} \cos \theta = \frac{K\lambda}{D} + 4\varepsilon \sin \theta, \quad (5)$$

where D is the crystalline size, K is the shape factor (0.94), λ is the wavelength of Cu$k\alpha$ radiation, θ is the Bragg angle, β_{hkl} is the full width at half maximum and ε is the crystalline strain.

Dispersion of crystalline strain and particle size for BFO, WO$_3$ and BFO–WO$_3$ with respect to the Bragg angle are shown in Fig. 3, and the corresponding values for each sample are tabulated in Table I.

Topographical Analysis on the Nanocomposites of BiFeO$_3$–WO$_3$

The electronic micrographs of BFO–WO$_3$ nanocomposites have been obtained from a field emission scanning electron microscope (FE-SEM) showing the actual particle size distribution and morphology of virgin BFO and BFO–WO$_3$ hybrid particles. It strongly depends on the synthesis temperature and method of approach. Figure 4a shows the SEM images of the virgin BFO

Fig. 2. XRD patterns of BiFeO$_3$, WO$_3$ and nano composites of BiFeO$_3$–WO$_3$.

Fig. 3. W–H plot of BiFeO$_3$, WO$_3$ and nano composites of BiFeO$_3$–WO$_3$.

Table I. Crystalline strain and size for BFO, WO₃ and BFO–WO₃

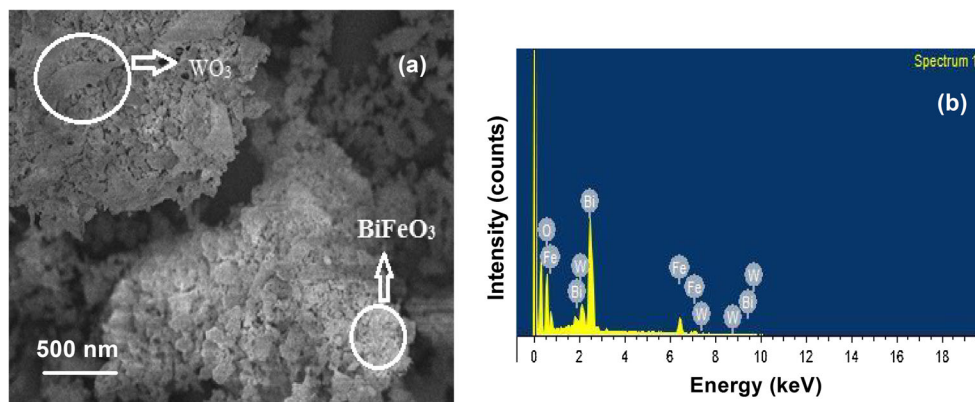| S. no.	Name of the photocatalyst	Crystalline size (nm)	Strain
1	$BiFeO_3$	80	6.07 E−2
2	WO_3	8	3.2 E−2
3	$BiFeO_3$–WO_3	32	4.2 E−2

Fig. 4. (a) Distribution of BFO and WO₃ particles in the BFO–WO₃ nanocomposites and (b) representing the EDX pattern of nanocomposites of BFO with WO₃.

nanoparticles synthesized through the sol–gel method. It can be seen that the composite samples are composed with a mixture of spherical particles accompanied by larger and elongated particles. BFO particle morphology appears to have been changed due to the binding concentration of WO₃ co-catalysts. The distinct particle size features of BFO and WO₃ observed in topographical images recorded for the nanocomposites ascertain the absence of any other impurities in the heterogeneous catalyst.[49] The results obtained from SEM pictures corroborates with the powder x-ray diffraction data. Figure 4b represents the energy dispersive x-ray analysis (EDX) data on the composition of elements present in the photocatalyst and it confirms the presence of WO₃ in a nanohybrid system.

SEM images further confirmed the presence of BFO spherical particles and as well as WO₃ particles as elongated ones. They are found to be agglomerated in nature. The observation made elsewhere[47] was totally contradictory for a BFO system loaded with CuS using hydrothermal synthesis, wherein it was noted that CuS exists as nanorods and BFO as nanoplates. However, the interfacial region between CuS and BFO was observed in a distinct mode. A similar kind of distinct feature in morphological texture of BFO and WO₃ has been noticed for the present case. In general, the formation of a heterojunction is normally responsible for the facial migration of excited electrons and holes in BFO–WO₃ based photocatalytic materials. The nanostructured elemental mapping from energy dispersive x-ray analysis (EDX) has also conveyed the fact that both photocatalysts BFO and WO₃ are uniformly distributed throughout the sample. Thus, the variation in the firing temperature required for the synthesis of BFO–WO₃ plays a vital role in deciding the admixtured morphological texture (spherical and elongated) of the newly formed nanocomposites.

Optical Absorption Measurements on BFO–WO₃ Nanohybrids

UV–Vis absorption spectra of the as-synthesized BFO and heterostructured BFO–WO₃ have been recorded at room temperature so as to investigate the influence of modification with WO₃ on the optical absorption properties of BFO. Figure 5a shows the maximum absorption pleateau of BFO nanoparticles ranging from 360 nm to 500 nm clearly indicating the ability of BFO to harvest visible solar radiation. This visible light harvesting behaviour of BFO has been further extended in the range of 340–510 nm through a modification of its phase with WO₃. The corresponding Tauc plots[50] confirms the direct band gap semiconductor nature of BFO–WO₃ and it is shown in Fig. 5b. The energy band gaps for BFO and BiFeO₃–WO₃ are of the order of ca. 1.8 eV and ca. 1.5 eV, respectively. As predicted earlier,[51] a broaden absorption in the visible region is attributed to the interband transition ($O_{2P}^{2-} \rightarrow Fe_{3d}^{3+}$) and absorption around the lower wavelength region (UV–near Vis) is due to ligand to metal charge transfer transition.
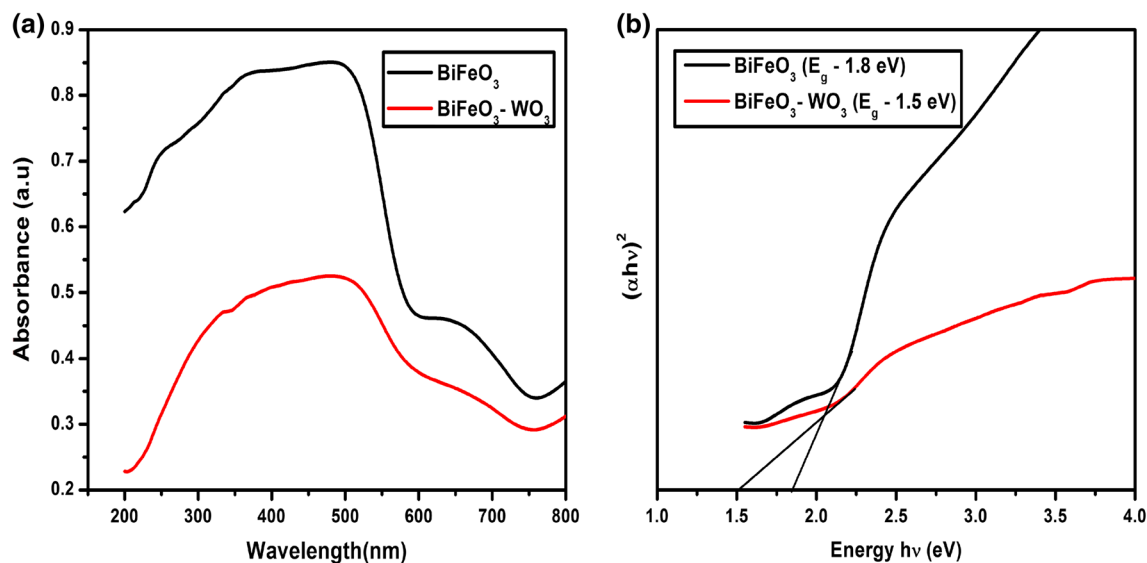
Fig. 5. (a) UV–Vis spectra of BFO and nanocomposites of BFO–WO$_3$ along with their (b) Tauc plots.

Table II. Comparative data on band gap energies and average particle sizes of heterogenous photocatalysts

S. no.	Name of the photocatalyst	Average particle size (nm)	Energy band gap (E_g) (eV)
1	BFO–graphene[25]	110	2.06
2	BiFeO$_3$–Bi$_2$Fe$_4$O$_9$[28]	210	2.1
3	Pt/BiFeO$_3$[29]	10	2.1
4	BiFeO$_3$–BiVO$_4$[30]	100	2.1
5	BFO–WO$_3$ (present work)	18	1.5

The optical absorption in the visible portion of light for BiFeO$_3$ loaded with WO$_3$ has considerably increased when compared to virgin BFO. An appreciable enhancement of absorption of light in the visible wavelengths provides a clue that BFO–WO$_3$ could probably be a better photocatalyst under visible light exposure. The band gap tuning (1.5 eV) upon WO$_3$ loading is quite consistent with the reported values[52–55] and it more appropriate than the virgin sample. As per the fruitful idea given by Li et al.,[56] in graphene–BFO composites, it was pointed out that the change in energy gap upon loading a catalyst with BFO is a key indicator for deciding the nature of interface coupling. The larger the difference in the E_g values, the higher will be the coupling. As such, a significant modification of E_g = 1.5 eV has been made in BFO–WO$_3$ composites over virgin BFO (E_g = 1.8 eV).Therefore, the prepared BFO–WO$_3$ nanocomposites shows a good sign for optimum interface coupling. The decrease in the band gap energy for BFO–WO$_3$ may be due to the fact that WO$_3$ addition would possibly be decreasing electronic correlation energy with oxygen vacancies introduced by the valence saturation of Fe^{3+} ions.[57] In general, BFO composite materials form hybridization with co-catalysts at the surface of BFO nanoparticles. Due to strong nature of covalent

bonds, charge transfer from oxygen ligand to Fe ions would further reduce the energy gap. Typical changes observed in E_g Values for various catalysts with BFO have been compared in the Table II.

Fourier Transform Infrared Spectroscopy (FTIR) Studies on BFO–WO$_3$ Nanocomposites

Fourier transform infrared spectroscopy (FTIR) spectra have been recorded for BFO and as well as for the nanocomposites of BFO–WO$_3$. In both spectra as shown in Fig. 6 two medium absorption peaks at ca. 455 cm^{-1} and 520 cm^{-1} could be observed. It corresponds to the overlapping Fe–O stretching and bending vibrations. It is also identified as the characteristic absorption FeO$_6$ octahedra of the perovskite structure.[58] A feeble peak at 711 cm^{-1} for BFO is attributed to the water absorption from the external atmosphere, and it is highlighted in the earlier report,[59] where the peak has been found less pronounced in the present BFO composite sample upon modification with WO$_3$ matrix. This would imply that composites of BFO–WO$_3$ rarely absorb atmospheric humidity.

A weak IR absorption observed around 1600–1630 cm^{-1} in both samples may be due to stretching vibrations of C=O (corresponding to the groups of

tartaric acid). A broad hump at ca. 1328 cm^{-1} with BFO would normally occur due to the symmetric bending vibrations of aliphatic C-H group. Further, some new peaks evoluted at ca. 715 cm^{-1}, 767 cm^{-1} and 829 cm^{-1} in BFO–WO$_3$ nanocomposite sample reflects the IR absorptions of W–O groups[59,60] and it was not seen in virgin BFO. This confirms the formation of WO$_3$ particles on the surface of the BFO nanomatrix. The band assignments for all possible IR absorptions to BFO, WO$_3$ and nanocomposites of BFO–WO$_3$ are tabulated in Table III.

Thermal Studies on BFO–WO$_3$ Nanocomposites

From thermogravimetric analysis (TGA)/differential thermal analysis (DTA) studies shown in Fig. 7a, it has been observed that the nanocomposites of BFO–WO$_3$ shows a weight loss of 55.4% in thermogravimetric analysis (TGA)/ trace around 840–880°C, and it corresponds to the partial decomposition of the title compound. The corresponding thermal event has also been indicated in differential thermal analysis (DTA) curves as a small hump at 870°C ascertaining the thermal stability of BFO–WO$_3$. Nearly at 910°C, the compound decomposes almost 98%, and the remaining carbon residues are
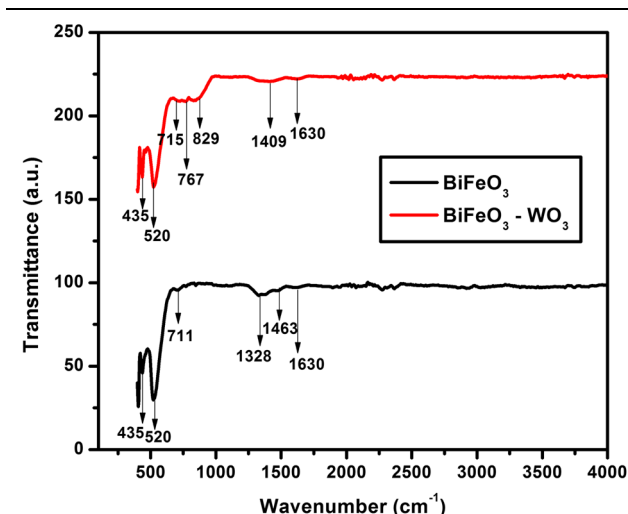
Fig. 6. FTIR spectra of BiFeO$_3$ and BiFeO$_3$–WO$_3$ nanocomposite.

left in the sample. No significant event could be observed between RT-800°C in differential thermal analysis (DTA) graphs. Therefore, it could be perceived that upon WO$_3$ modification with BFO, the nanocomposite sample appear to be losing ferroelectric/antiferromagnetic characters. In order to substantiate the observed result in Fig. 7b, a vibrating-sample magnetometer (VSM) signal was recorded with respect to a magnetic field, and it implies that the loading of WO$_3$ with BFO found to have suppressed the multiferroic character of the nanocomposites. This could be clearly observed from a vibrating-sample magnetometer (VSM) and no loop-like structure is experimented for the BFO–WO$_3$ sample. Further, it has also been inferred that modification of BFO with WO$_3$ has considerably lowered its thermal withstanding limit, as it decomposes before it melts.

Photocatalytic Dye Degradation Activity of BFO–WO$_3$ Nanocomposites

A natural sunlight emitting UV and visible radiation over the range 300–700 nm was used as the light resource instead of a solar simulator. In a typical test, 10 mg of the as-prepared photocatalysts was fed in a 10 mL solution containing Methylene Blue (10 mg/L). The reaction mixture (suspension) was stirred for 2 h under dark conditions to realize the adsorption equilibrium. Then the solution was irradiated in natural sunlight during the daytime between 10 AM to 3 PM (temperature ranging 30–33°C) under continuous stirring. The relative concentration of Methylene blue (MB) in the treated solution was subsequently analyzed by UV–Vis–NIR spectroscopy at regular time 3 h intervals. Virgin BFO and WO$_3$ were used as a photocatalytic reference to evaluate activity of the BiFeO$_3$–WO$_3$ nanocomposites.

Photocatalytic properties to a series of powders of BiFeO$_3$, WO$_3$ and nanocomposites of BFO–WO$_3$ have been studied by monitoring the decomposition of the methylene blue (MB) in aqueous solution under sunlight. MB is stable under UV–Vis irradiation, if no photocatalyst is involved. Pure BFO exhibits inherent photocatalytic activity in the UV and visible light region and about 76% of the MB solution was photodegraded in 9 h. It has been shown in Fig. 8a. Similarly, photodegradation

Table III. Band assignments for all possible IR absorptions to BFO, WO$_3$ and nanocomposites of BFO–WO$_3$

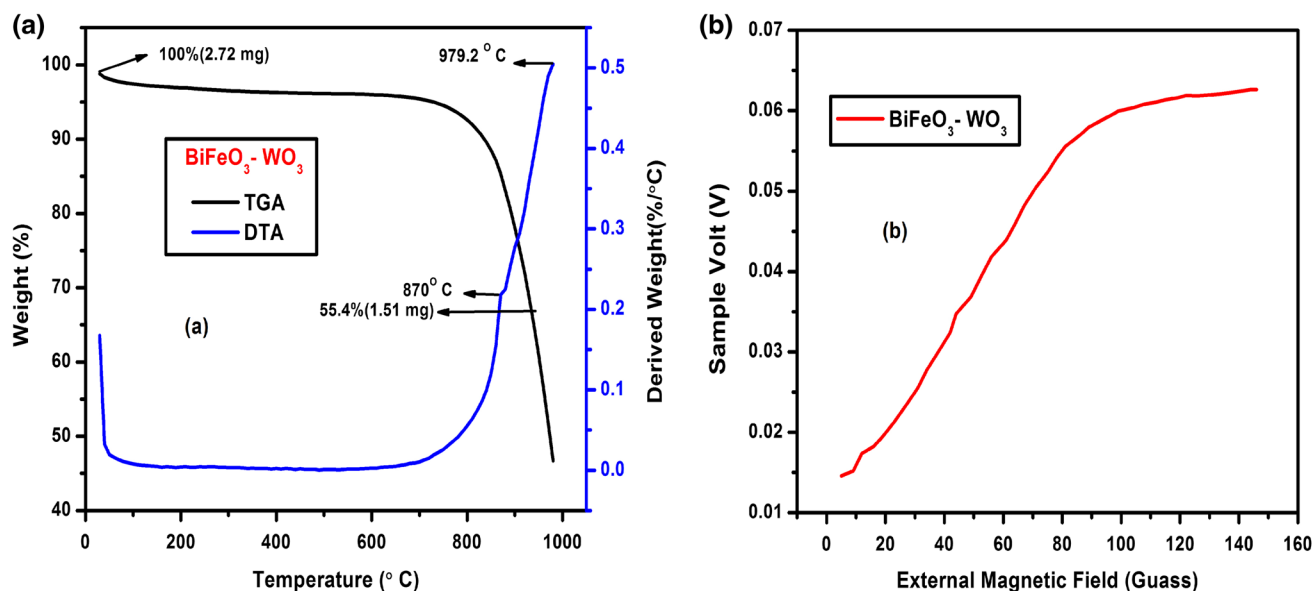| S. no.	IR absorptions (cm^{-1})	Band assignments
1	455 and 520	Fe–O stretching and bending vibrations
2	711	Water absorption
3	1600–1630	Stretching vibrations of C=O
4	1328	Bending vibrations of aliphatic C–H group
5	715, 767 and 829	W–O groups

(a)

(b)

Fig. 7. (a) TGA–DTA trace of BFO–WO$_3$ nanocomposites, (b) VSM graph of BFO–WO$_3$ nanocomposites.

action of WO$_3$ (59%) has also been analysed, and it is shown in Fig. 8b in order to evaluate the influence of WO$_3$ particles in modifying the dye degradation properties of BFO–WO$_3$. Due to the reduction in the band-gap of BFO after binding with WO$_3$ powder, it shows a higher photocatalytic activity in the preferred visible light region, when compared with virgin BFO samples. With the assistance of WO$_3$ powders, nearly 91% of the MB solution was degraded by BFO–WO$_3$ nanocomposites under sunlight within the same reaction time of 9 h. It has been indicated in Fig. 8c and d. This may be due to the fact that the recombination rate of the charge carriers increases exponentially with the composite concentration, consequent to the average distance between trap sites decreases with an increase of binder restricted within a particle. To quantitatively analyze the reaction kinetics of MB degradation, the pseudo-first-order equation according to Langmuir–Hinshelwood model[62] was applied, and it can be expressed by the following equation

$$\ln\left(C_0/C_t\right) = kt, \qquad (6)$$

where C_0 and C_t are the concentrations of MB (mg L^{-1}) at different irradiation time of 0 and t, respectively. 'k' is the pseudo-first-order rate constant of photodegradation (min^{-1}). From Fig. 8e, the linear fitting curves of ln (C_0/C_t) versus irradiation time (t) show a better correlation to pseudo-first-order reaction kinetics for BFO–WO$_3$ photocatalyst over the other ones. The first order kinetic constant value was analyzed for all samples, and the values of R^2 have been tabulated in Table IV. Photocatalytic degradation efficiency has also been estimated both for the parent and nanocomposite

particles using Eq. 7. The variation in the efficiencies for BFO–WO$_3$ is shown in Fig. 8f.

$$\text{Efficiency } \eta = \frac{(C_0 - C_t)}{C_0} * 100\% \qquad (7)$$

The stability of BiFeO$_3$–WO$_3$ samples has been verified with a consecutive trail run of 3 cycles @ 9 h/cycle with a total of 27 h. The composites were found to be very stable. It was ensured that the stability remain unchanged till the completion of the 3rd run.

The samples recovered after every cycle, using centrifugation from the aqueous medium and dried in an oven for 4 h. The dried recovered sample can be reused again for the photodegradation methylene blue solution under natural sunlight which ran for another 9 h. This has been repeated for three cycles. The absorbance values are same in all cycles. The graph indicating reusability of composites is shown in Fig. 8g.

A comparative picture of dye degradation activity of relevant heterogeneous oxide photocatalysts is shown in Table V, wherein it can be inferred that the performance of the title compound appears to be far better than some of the literature reports.

Photocatalytic Mechanism Involved in BFO–WO$_3$ Nanocomposites

It is perceived from literature reports[60–62] that virgin BFO is capable of generating excitons upon the absorption of visible light and paves the way for driving the photocatalytic degradation of MB. Herein, the mechanism of enhanced photocatalytic activity of BiFeO$_3$(BFO)/WO$_3$ heterogeneous
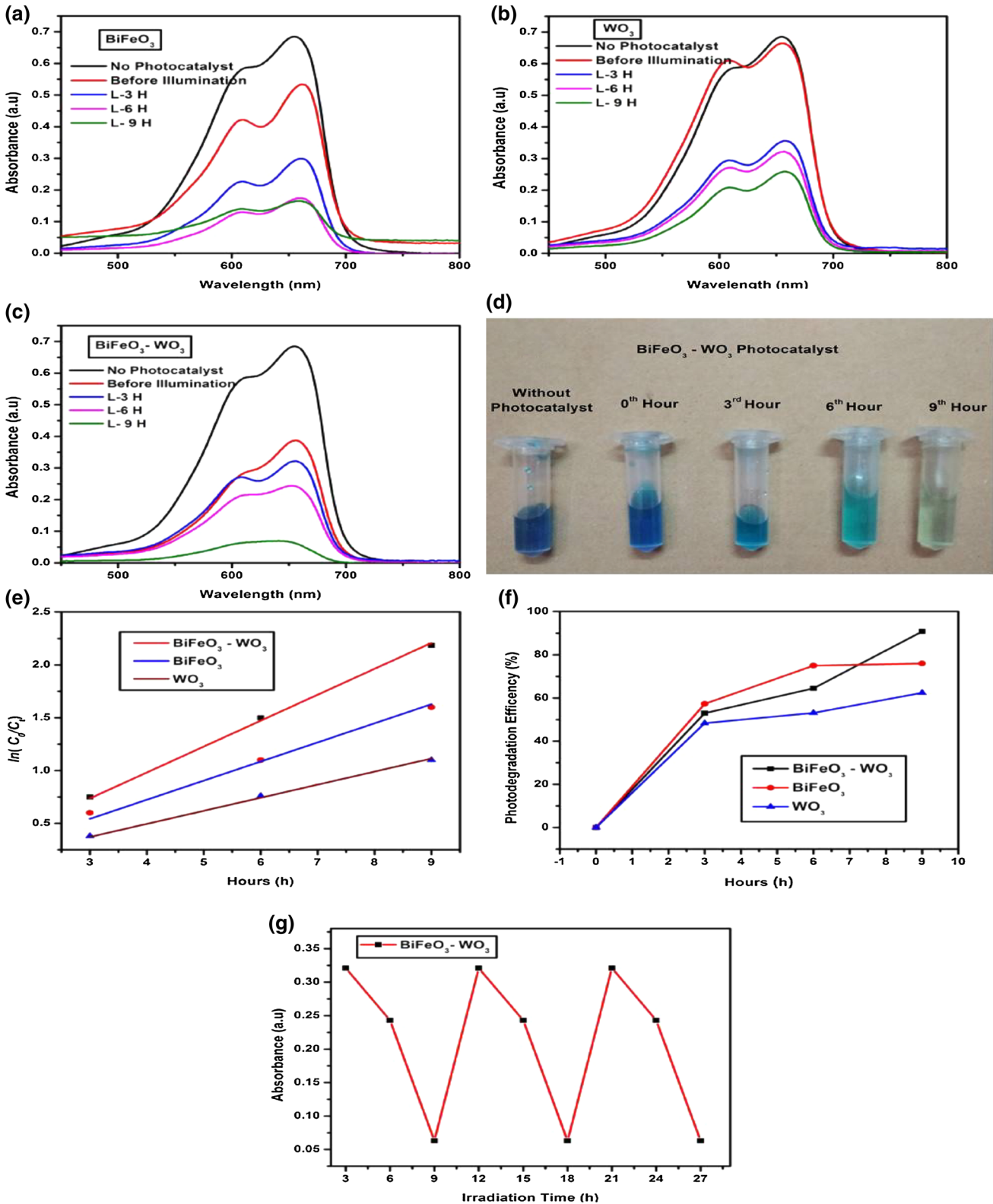
Fig. 8. (a) Variation in the concentration of dye degradation of MB with respect to wavelength for $BiFeO_3$, (b) variation in the concentration of dye degradation of MB with respect to wavelength for WO_3, (c) variation in the concentration of dye degradation of MB with respect to wavelength for $BiFeO_3$–WO_3, (d) degradation of methylene blue using BFO–WO_3 nanocomposites, (e) exposure time versus ln (C_0/C_t) for BFO, WO_3 and nanocomposites of BFO–WO_3, (f) exposure time versus photodegradation efficiencies BFO, WO_3 and BFO–WO_3 nanocomposites and (g) stability of dye absorbance versus exposure time to BFO–WO_3 nanocomposites after 3 cycles @ 9 h.

Table IV. Comparison of rate constants for various photocatalysts with BFO–WO₃ and their corresponding goodness of fit values

Estimated values of first order kinetic constants for BFO, WO₃ and BFO–WO₃ solution with methylene blue

S. no.	Photocatalyst	Slope K (min^{-1})	Standard error	R value	R^2 value
1.	BiFeO₃	0.18095	0.00412	0.99948	0.99948
2.	WO₃	0.1238	0.0015	0.99985	0.99956
3.	BiFeO₃–WO₃	0.2453	0.00241	0.99992	0.99971

Table V. Comparative analysis on the dye degradation efficiencies of a few heterogenous photocatalyts

S. no.	Name of heterogeneous catalyst	Degradation efficiency (%)	Time (h)
1	SiO₂–WO₃[41]	37	3
2	BiFeO₃/MOF nanocomposite[32]	48	3
3	CuO–BiVO₄[17]	40	3
4	BiFeO₃/WO₃ (present work)	54	3

nanostructure compared to the virgin BiFeO₃ and WO₃ can be ascribed for the formation of the p–n junction between p-type BiFeO₃ and n-type WO₃ semiconductors.

The valance band (VB) and conduction band (CB) positions for the virgin BiFeO₃ and WO₃ were calculated using the Mullikan electronegativity method as per the following steps.

$$E_{VB} = X + 0.5E_g - 4.5\,(E_e), \tag{8}$$
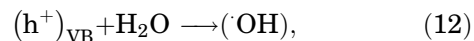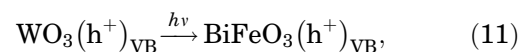
$$E_{CB} = E_{VB} - E_g, \tag{9}$$

where E_{VB} and E_{CB} are the valence and conduction band potential [w.r.t Normal Hydrogen Electrode (NHE)], X is the electronegativity of the semiconductor, E_e is the energy of free electron on hydrogen scale (4.5 eV), and E_g is the band gap of the photocatalyst. (BiFeO₃ $\sim$ 1.5 eV and WO₃ $\sim$ 2.4 eV).

It has been computed that the conduction band (CB) and valence band (VB) potentials of the BiFeO₃ semiconductor (serves as p-type) are 0.4 eV and 2.2 eV and for the WO₃ semiconductor (serves as n-type) they are 0.8 eV and 3.2 eV, respectively.

Figure 9 shows the energy-band schematic diagram for p-type BFO and n-type WO₃. Thus, before the formation of a junction layer, the conduction band edge of p-type BiFeO₃ is higher than that of n-type WO₃. After the formation of BiFeO₃ and WO₃, the whole energy band of BiFeO₃ is raised up, while that of WO₃ is in decline and as a result, the conduction band edge of BiFeO₃ is much higher than that of WO₃. Thus at the equilibrium, an inner electric field from n-type WO₃ to p-type BiFeO₃ is established. Under visible-light irradiation, both BiFeO₃ and WO₃ can be excited to generate electron–hole pairs. According to the energy band schematic diagram in Fig. 9, the photogenerated electron of the conduction band of the p-type BiFeO₃ can transfer to that of n-type WO₃. It has been reported[63] that whenever the electrons react with W^{6+} species in the WO₃, W^{6+} will be reduced into W^{5+}. The W^{5+} ions in the surface of WO₃ can be re-oxidized into W^{6+} through the reaction with oxygen to generate superoxide radical ($\cdot$O$_2^-$). Superoxide radical ($\cdot$O$_2^-$) can also react with H₂O molecules to form .OH. Hydroxyl radical (.OH) and superoxide radical ($\cdot$O$_2^-$) are the main species to degrade MB into CO₂ and H₂O under visible light irradiation. As such, in this case, the holes tend to remain in the BiFeO₃ valence band, while simultaneously photo-generated holes can migrate from the valence band of n-type WO₃ to that of p-type BiFeO₃. The migration of photogenerated carriers can further be promoted by the internally formed electric field. Therefore, the photogenerated electrons and holes could be effectively separated by the p–n junction formed between the p-type BiFeO₃ and n-type WO₃ interface so that the recombination of electron-hole pairs can be substantially reduced.

Successive mechanisms are involved in the photodye degradation of BFO/WO₃ composite
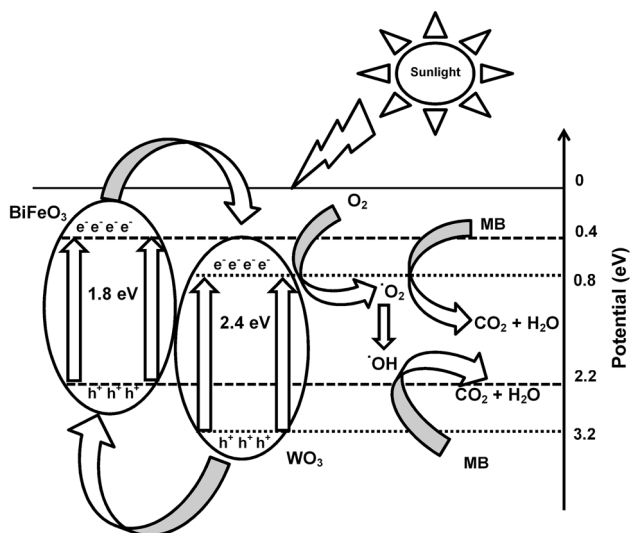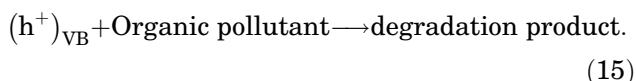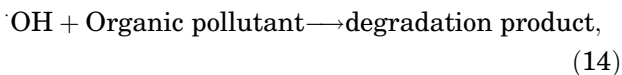
$$\mathrm{BiFeO_3(e^-)_{CB}} \xrightarrow{h\nu} \mathrm{WO_3(e^-)_{CB}}, \tag{10}$$

$$\mathrm{WO_3\left(h^+\right)_{VB}} \xrightarrow{h\nu} \mathrm{BiFeO_3\left(h^+\right)_{VB}}, \tag{11}$$

$$\left(\mathrm{h^+}\right)_{VB} + \mathrm{H_2O} \longrightarrow (\cdot\mathrm{OH}), \tag{12}$$

$$(\mathrm{e^-})_{CB} + \mathrm{O_2} \longrightarrow \left(\cdot\mathrm{O_2^-}\right) + \mathrm{H_2O} \longrightarrow \cdot\mathrm{OH} + \mathrm{OH^-}, \tag{13}$$

Fig. 9. The energy-band schematic diagram for *p*-type BFO and *n*-type WO$_3$.

$$^{\cdot}\text{OH} + \text{Organic pollutant} \longrightarrow \text{degradation product}, \quad (14)$$

$$\left(\text{h}^+\right)_{\text{VB}} + \text{Organic pollutant} \longrightarrow \text{degradation product}. \quad (15)$$
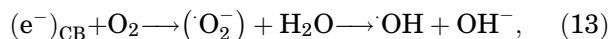
Thus, the separated electrons and holes are free to initiate reactions with the reactants adsorbed on the photocatalyst surface, leading to an enhanced photocatalytic activity. One of the most striking reasons for enhancing the photocatalytic efficiency of BFO/WO$_3$ is capturing the aromatic ring of methylene blue due to higher surface area contact in nanocomposite samples as compared with virgin BFO and WO$_3$ samples.

CONCLUSION

Nanocomposites of newly formed BFO–WO$_3$ have been successfully synthesized through a sol–gel single step process. The PXRD pattern obtained for BFO–WO$_3$ confirms the existence of the diffraction peaks corresponding to both WO$_3$ and BiFeO$_3$. Observation of FESEM images also suggest that there exists two different morphologies of particles viz., spherical type indicating the BFO nanoparticles and elongated structured ones are WO$_3$ in nature. Upon WO$_3$ loading with BFO photocatalyst, reduction in the band gap energy found to have been noticed from 1.8 eV (BFO) to 1.5 eV (BFO–WO$_3$), and this has extended the optical absorption range of the compound for the entire visible region. FTIR measurements reveal that the vibrational structure of nanocomposite contains IR absorptions of both moieties. Thermal and VSM studies present the fact that the multiferroic character of BFO was found to be suppressed when loaded with WO$_3$ photocatalyst.

However, photocatalytic dye degradation activity of BFO–WO$_3$ on methylene blue dye was enhanced to 91% when compared to pure BFO (76%) and WO$_3$ (59%) under the same experimental conditions. The stability of the composite recurs for every 9 h reveals that the title compound could be a reusable one and perhaps BFO–WO$_3$ will be a potential candidate for the efficient removal of MB effluent.

REFERENCES

1. A. Mills, R.H. Davies, and D. Worsley, *Chem. Soc. Rev.* 22, 417 (1993).
2. K. Honda and A. Fujishima, *Nature* 238, 37 (1972).
3. C. Michel, J.M. Moreau, G.D. Achenbach, R. Gerson, and W.J. James, *Solid State Commun.* 7, 701 (1969).
4. H. Wang, X. Fei, L. Wang, Y. Li, S. Xu, M. Sun, L. Sun, C. Zhang, Y. Li, Q. Yang, and Y. Wei, *New J. Chem.* 35, 1795 (2011).
5. M. Bilal Tahir, S. Hajra, N.R. Khalid, M. Rizwan, and G.N. Watto, *J. Inorg. Organomet. Polym.* 28, 1 (2018).
6. N.R. Khalid, M. Liaqat, M. Bilal Tahir, G. Nabi, T. Iqbal, and N.A. Niaz, *Ceramic Int.* 44, 546 (2018).
7. A. Fujishima, X. Zhang, and D.A. Tryk, *Surf. Sci. Rep.* 63, 515 (2008).
8. C.T. Meng, R. John, N.S. Wei, and J. Bing, *J. Mol. Syst. Des. Eng.* 2, 449 (2017).
9. J. Zhang, R. He, and X. Liu, *Nanotechnology* 24, 505401 (2013).
10. Z. Jindal and N.K. Verma, *Physica E* 43, 1021 (2011).
11. W. Qizhao, L. Jiajia, B. Yan, L. Juhong, H. Haohao, L. Zhimin, L. Ziqiang, and S. Wenfeng, *Green Chem.* 16, 2728 (2014).
12. T. Soltani and M.H. Entezari, *J. Mol. Catal. A Chem.* 377, 197 (2013).
13. S.M. Lam, J.C. Sin, and A.R. Mohamed, *Mater. Res. Bull.* 90, 15 (2017).
14. S. Shabani, S.M. Mirkazemi, S.M. Masoudpanah, and P.T. Dolat Abadi, *J. Supercond. Nov. Magn.* 27, 2795 (2014).
15. F. Gao, X.Y. Chen, K.B. Yin, S. Dong, Z.F. Ren, F. Yuan, T. Yu, Z.G. Zou, and J.M. Liu, *Adv. Mater.* 19, 2889 (2007).
16. D. Wang, G. Xue, Y. Zhen, F. Fu, and D. Li, *J. Mater. Chem.* 22, 4751 (2012).
17. J. Jiang, K. Zhao, X. Xiao, and L. Zhang, *J. Am. Chem. Soc.* 134, 4473 (2012).
18. K. Villa, S. Murcia-López, J.R. Morante, and T. Andreu, *Appl. Catal.* 187, 30 (2016).
19. S. Thiyagarajan, S. Singh, and D. Bahadur, *Mater. Chem. Phys.* 173, 385 (2016).
20. X. Xiaoli, L. Xiao, Y. Ji, Y. Hong, J. Ma, and Z. Wu, *J. Electron. Mater.* 47, 536 (2018).
21. C. Ponraj, G. Vinitha, and J. Daniel, *Environ. Nanotechnol. Monit. Manag.* 7, 110 (2017).
22. S. Chatterjee, A. Bera, and A.J. Pal, *ACS Appl. Mater. Interfaces* 6, 20479 (2014).
23. L. Lu, M. Lv, G. Liu, and X. Xu, *Appl. Surf. Sci.* 391, 535 (2017).
24. S.J.A. Moniz, D. Pugh, C.S. Blackman, J. Tang, and C.J. Carmalt, *Cryst. Growth Des.* 16, 3818 (2016).
25. S. Irfan, L. Li, A.S. Saleemi, and C.-W. Nana, *J. Mater. Chem. A* 5, 11143 (2017).

26. R. Marschall, *Adv. Funct. Mater.* 24, 2421 (2014).
27. R. Guo, L. Fang, W. Dong, F. Zheng, and M. Shen, *J. Mater. Chem.* 21, 18645 (2011).
28. B. Safizade, S.M. Masoudpanah, M. Hasheminiasari, and A. Ghasemi, *RSC Adv.* 8, 6988 (2018).
29. Y.P. Bhoi, S.R. Pradhan, C. Behera, and B.G. Mishra, *RSC Adv.* 6, 35589 (2016).
30. H. Ramezanalizadeh and F. Manteghi, *J. Photochem. Photobiol. A Chem.* 338, 60 (2017).
31. X. Wang, W. Mao, J. Zhang, Y. Han, C. Quan, Q. Zhang, T. Yang, J. Yang, X. Li, and W. Huang, *J. Colloid Interface Sci.* 448, 17 (2015).
32. T. Fan, C. Chen, Z. Tang, Y. Ni, and C. Lu, *Mater. Sci. Semicond. Process.* 40, 439 (2015).
33. X. Wang, H. Hu, S. Chen, K. Zhang, J. Zhang, W. Zou, and R. Wang, *Mater. Chem. Phys.* 158, 67 (2015).
34. Y.P. Bhoi, C. Behera, D. Majhi, Sk.Md. Equeenuddin, and B.G. Mishra, *New J. Chem.* 42, 281 (2018).
35. M. Miyauchi, M. Shibuya, Z. Zhao, and Z. Liu, *J. Phys. Chem. C* 113, 10642 (2009).
36. B. Weng, J. Wu, N. Zhang, and Y. Xu, *Langmuir* 30, 5574 (2014).
37. P. Wang, Y. Bai, P. Luo, and J. Liu, *Catal. Commun.* 38, 82 (2013).
38. Z. Sun, T. Liao, Y. Dou, S. Hwang, M. Park, L. Jiang, J. Kimand, and S. Dou, *Nat. Commun.* 5, 3813 (2014).
39. J. Liu, O. Margeat, W. Dachraoui, X. Liu, M. Fahlmanand, and J. Ackermann, *Adv. Funct. Mater.* 24, 6029 (2014).
40. J. Zhao, Z. Jia, X. Shen, H. Zhou, and L. Ma, *Ceram. Int.* 41, 5600 (2015).
41. S.A.K. Leghari, S. Sajjad, and J. Zhang, *RSC Adv.* 3, 15354 (2013).
42. C.W. Lai and S. Sreekantan, *Int. J. Hydrogen Energy* 38, 2156 (2013).
43. B. Sivakumar, S. Mohan, and B. Subramanian, *J. Phys. Chem. C* 120, 18811 (2016).
44. S. Bharathkumar, M. Sakar, K. Rohith Vinod, and S. Balakumar, *Phys. Chem. Chem. Phys.* 17, 17745 (2015).
45. M. Sakar, S. Balakumar, P. Saravanan, and S. Bharathkumar, *Nanoscale* 8, 1147 (2016).
46. V.V. Zuev, S.N. Grigoriev, R.I. Romanov, V.Y. Fominski, M.A. Volosova, and M.V. Demin, *J. Phys. Conf. Ser.* 747, 012050 (2015).
47. Y.P. Bhoi and B.G. Mishra, *Chem. Eng. J.* 344, 391 (2018).
48. V.D. Mote, Y. Purushotham, and B.N. Dole, *J. Theor. Appl. Phys.* 6, 6 (2012).
49. W.-H. Hu, G.-Q. Han, B. Dong, and C.-G. Liu, *J. Nanomater.* (2015). https://doi.org/10.1155/2015/346086.
50. S. Godara, N. Sinha, and B. Kumar, *Int. J. ChemTech Res.* 6, 2083 (2014).
51. T. Soltani and B.K. Lee, *Chem. Eng. J.* 306, 204 (2016).
52. I.T. Papadas, S.S. Kota, M.G. Kanatzidis, and G.S. Armatas, *Nanoscale* 13, 5737 (2015).
53. T. Zhang, Y. Shen, Y. Qiu, Y. Liu, R. Xiong, J. Shi, and J. Wei, *ACS Sustain. Chem. Eng.* 5, 4630 (2017).
54. T. Fan, C. Chen, and Z. Tang, *RSC Adv.* 6, 9994 (2016).
55. Y.P. Bhoi, C. Behera, D. Majhi, S.M. Equeenuddin, and B.G. Mishra, *New J. Chem.* 42, 281 (2018).
56. Z. Li, Y. Shen, Y. Guan, Y. Hu, Y. Lin, and C.W. Nan, *J. Mater. Chem. A* 2, 1967 (2014).
57. T. Higuchi, Y.S. Liu, P. Yao, P.A. Glans, and J. Guo, *Phys. Rev. A* 78, 085106 (2008).
58. M. Arora, P.C. Sati, S. Chauhan, S. Chhoker, A.K. Panwar, and M. Kumar, *J. Supercond. Nov. Magn.* 26, 443 (2013).
59. U. OparaKrašovec, A. ŠurcaVuk, and B. Orel, *Electrochim. Acta* 13, 1921 (2001).
60. T. Gao, Z. Chen, Y. Zhu, F. Niu, Q. Huang, L. Qin, X. Sun, and Y. Huang, *Mater. Res. Bull.* 59, 6 (2014).
61. K. Vasanth Kumar, K. Porkodi, and F. Rocha, *Catal. Commun.* 9, 82 (2008).
62. J. He, R. Guo, L. Fang, W. Dong, F. Zheng, and M. Shen, *Mater. Res. Bull.* 48, 3017 (2013).
63. P. Wang, N. Lua, S. Yan, N. Liu, Yu Hongtao, J. Li, and W. Yan, *Appl. Surf. Sci.* 423, 197 (2017).